

# Airfoil Diffusion: synthesizing airfoils for desired performance characteristics

**Reid Graves**

Department of Mechanical Engineering,  
Carnegie Mellon University,  
5000 Forbes Avenue,  
Pittsburgh, PA, 15213  
email: barati@cmu.edu

**Amir Barati Farimani**<sup>1</sup>

Department of Mechanical Engineering,  
Carnegie Mellon University,  
5000 Forbes Avenue,  
Pittsburgh, PA, 15213  
email: barati@cmu.edu

*The design of aerodynamic shapes, such as airfoils, has traditionally required significant computational resources and relied on predefined design parameters, which limit the potential for novel shape synthesis. In this work, we introduce a data-driven methodology for airfoil generation using a diffusion model. Trained on a dataset of preexisting airfoils, our model can generate an arbitrary number of new airfoils from random vectors, which can be conditioned on specific aerodynamic performance metrics such as lift ( $C_L$ ) and drag ( $C_D$ ), or geometric criteria. Our results demonstrate that the diffusion model effectively produces airfoil shapes with realistic aerodynamic properties, offering substantial improvements in efficiency, flexibility, and the potential for discovering innovative airfoil designs. This approach significantly expands the design space, facilitating the synthesis of high-performance aerodynamic shapes that transcend the limitations of traditional methods.*

*Keywords: deep learning, diffusion model, airfoil design, generative models*

## 1 Introduction

The design and optimization of aerodynamic shapes, particularly airfoils, are fundamental challenges in aerospace engineering. Traditionally, the process of designing airfoils has relied heavily on computationally intensive simulations to explore the vast design space [1,2]. This approach typically involves defining specific design parameters that can limit the ability to synthesize truly novel shapes [3]. As the demand for higher performance and more efficient aerodynamic structures increases, there is a growing need for advanced methodologies that can streamline the design process and facilitate the generation of innovative airfoil geometries [4].

Recent advances in machine learning have opened new avenues for the design and optimization of complex systems [5]. Data-driven approaches, such as generative models, have shown promise in various fields by learning from existing data to generate new high-quality samples [6,7]. In the context of airfoil design, these models can potentially revolutionize the way we approach shape optimization by learning the underlying distribution of airfoil geometries and their aerodynamic properties [3,8,9].

In this work, we propose a novel methodology for airfoil generation using a diffusion model. Using a pre-existing dataset of 2 dimensional airfoils, we train a diffusion model that synthesizes novel airfoil profiles.

The diffusion model, once trained, allows for the generation of new airfoil shapes from random vectors. This capability enables the synthesis of new airfoils that can be selected on the basis of desired  $C_L$  and  $C_D$  values or particular geometric criteria. Our approach offers a data-driven framework that not only enhances the efficiency of the airfoil design process, but also has the potential to discover novel shapes with superior aerodynamic performance.

This paper is structured as follows. Section 2 provides an overview of related work in the field of generative models for aerodynamic design. Section 3 details the methodology, including the architecture of airfoil diffusion and the training process of diffusion models. Section 4 presents the results of our experiments that demonstrate the effectiveness of our approach. Finally, Section 5 concludes the paper and discusses potential future work.

## 2 Related Work

We propose a novel approach to airfoil design using conditional diffusion models that build upon existing methodologies in geometric parameterization and deep learning.

**2.1 Geometry Parameterization.** Traditional airfoil design has predominantly relied on computational simulations and fixed design parameters, which can restrict the exploration of innovative aerodynamic shapes [10]. These conventional methods, though effective in specific scenarios, often limit the ability to fully explore the expansive design space necessary for optimizing aerodynamic structures [4]. This limitation arises primarily from the need for predefining the design space using specific shape parameters, such as camber and thickness, which can constrain the range of possible geometries that can be considered during optimization.

To address these limitations, there has been a shift towards advanced machine learning techniques that allow for more flexible and efficient exploration of the design space. These approaches, including techniques like Bézier and B-spline parameterizations, offer greater control over airfoil geometry by representing shapes with a set of control points that can be adjusted to generate smooth and continuous surfaces. Such methods have been integrated into optimization frameworks to enhance the precision of geometric design while maintaining smoothness and manufacturability [11,12]. However, while these traditional geometric parameterizations provide a level of flexibility, they still require significant manual intervention and are often limited in handling highly complex shapes, especially in high-dimensional design spaces.

The introduction of data-driven methods, particularly deep learning models, has further advanced the field of geometry parameterization. By learning from large datasets of existing airfoil shapes, these models can generate new designs that meet specific aerodynamic performance criteria without being constrained by traditional shape parameters. Variational Autoencoders (VAEs) and Generative Adversarial Networks (GANs) have been particularly impactful in this domain. For example, the work by Li et al. [13] demonstrated the application of GANs to generate a diverse set of airfoil shapes by encoding them into a latent space, thereby enabling a more extensive exploration of the design space compared to traditional methods.

Moreover, Diffusion Models, as explored in recent studies, rep-

<sup>1</sup>Corresponding Author.

Version 1.18, August 29, 2024

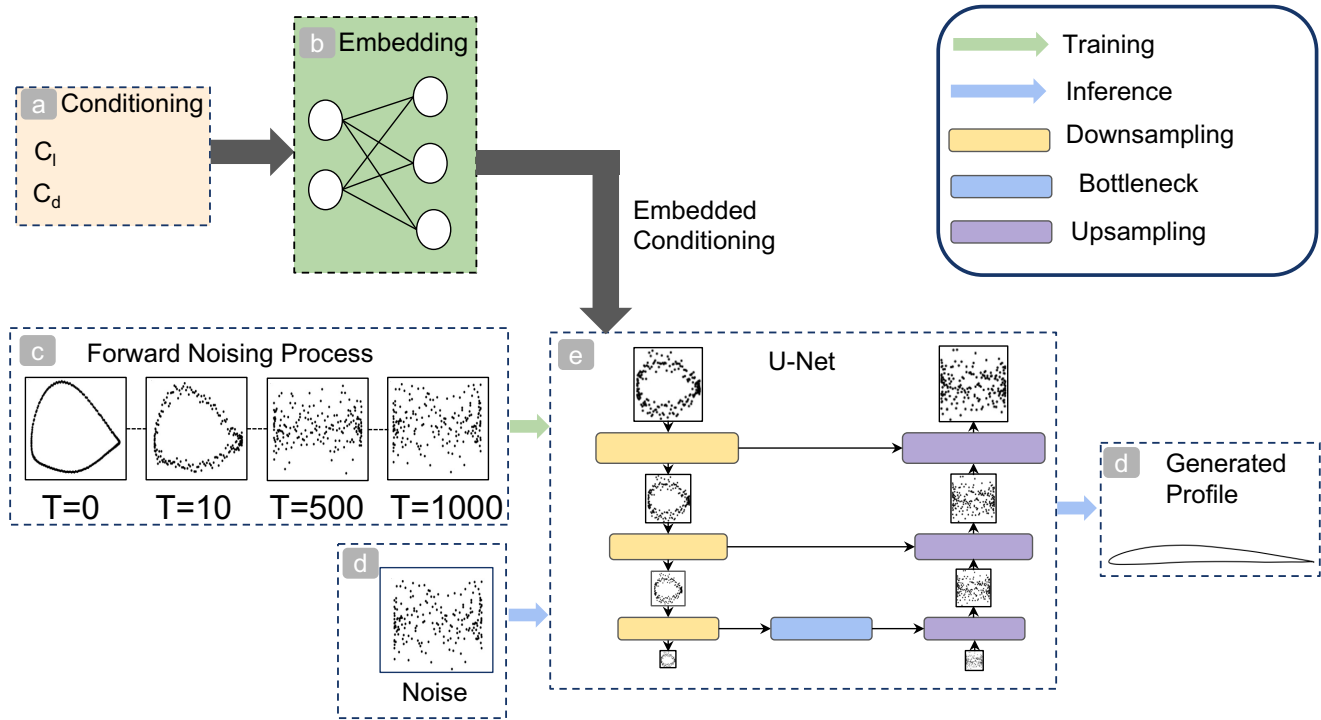


**Fig. 1 Overview of the Airfoil Diffusion Model:**

**a) Airfoil conditioning information such as the coefficient of lift ( $C_l$ ), coefficient of drag ( $C_d$ ), maximum thickness, and maximum camber is passed through b) conditional embedding multi-layer perceptron (MLP) layers. The embedded conditioning information is passed to e) the denoising U-Net. During training, samples are progressively distorted to approximate Gaussian noise, as shown in c). In the inference phase, a noise vector d) along conditioning value embedding are input to the U-Net e), which outputs the conditionally generated airfoil profile in d).**

represent a significant advancement in airfoil geometry parameterization. These models operate within a learned latent space, allowing for the generation of airfoil shapes with fewer training samples and maintaining high-quality outputs [14]. The ability of Diffusion Models to integrate specific design constraints directly into the generative process provides a powerful tool for optimizing aerodynamic shapes in a data-efficient manner.

As the field continues to evolve, hybrid approaches that combine traditional geometric parameterization with advanced machine learning techniques are emerging. These methods aim to leverage the strengths of both worlds—preserving the smoothness and manufacturability of traditional parameterizations while exploiting the flexibility and data-driven insights of deep learning models. The ongoing research in this area focuses on refining these techniques to accommodate increasingly complex aerodynamic and geometric constraints, ultimately pushing the boundaries of what is possible in airfoil design.

**2.2 Deep Learning Approaches.** Generative models, including Variational Autoencoders (VAEs) and Generative Adversarial Networks (GANs), have shown considerable promise in optimizing airfoil design by overcoming the limitations of traditional design methods. For instance, the Airfoil GAN model [3] encodes existing airfoil shapes into latent vectors, enabling the generation of novel airfoils with specific aerodynamic properties, without relying on predefined design parameters. This approach not only facilitates the exploration of high-dimensional design spaces but also integrates a genetic algorithm for optimizing aerodynamic performance, allowing the synthesized airfoils to evolve towards desired properties. Moreover, the model’s ability to generate smooth and realistic airfoils directly from the latent space, coupled with its interpretability through feature clustering, sets it apart from traditional techniques. In comparison, the use of free-form deformation generalized adversarial networks (FFD-GAN) [8] has advanced the

parameterization of three-dimensional aerodynamic shapes, yet it often requires predefined design formulations, limiting its flexibility in exploring novel geometries. The Airfoil GAN’s potential for application to other aerodynamic and engineering domains further underscores its significance in the field of design optimization.

Despite their potential, GAN-based methods often face challenges related to training stability and the need for large datasets. Addressing these issues, DiffAirfoil [15] introduces a novel approach that leverages a diffusion model within a learned latent space, specifically tailored for aerodynamic shape optimization. This model significantly enhances data efficiency, requiring substantially fewer training geometries compared to GANs, while still generating high-quality and diverse airfoil samples. The diffusion process not only ensures stable training and robust sampling, even under data-scarce conditions, but also mitigates the common pitfalls associated with adversarial training, such as mode collapse.

Moreover, DiffAirfoil’s conditional variant offers a distinct advantage in generating airfoils that meet specific geometric constraints without the need for retraining or model adjustments, thereby providing greater flexibility and efficiency in the design process. This capability is particularly valuable in scenarios where rapid design iterations are necessary, as it allows for the direct incorporation of user-defined constraints, such as maximum thickness or area, into the generated airfoil profiles.

However, DiffAirfoil’s approach is inherently tied to the use of a latent space for diffusion, where the model operates on latent vectors derived from an autoencoder. This methodology necessitates a template airfoil profile as a starting point, with the generated airfoils being deformed versions of this template, shaped according to the sampled latent vector. Although this approach is effective for optimizing and blending existing designs, it is fundamentally constrained by the reliance on predefined templates, which may limit the model’s ability to fully explore the design space and discover novel and unconventional airfoil geometries.

In contrast, our work advances deep learning methodologies by proposing a conditional diffusion model that operates directly in the airfoil geometric space, without the need for latent space transformations or template geometries. By avoiding the constraints of template-based generation, our model focuses on the exploration of the design space rather than the optimization of existing designs. This approach enables our model to learn a comprehensive representation of the entire training dataset and generates airfoils that are not bound by the limitations of pre-existing shapes. Consequently, our model is more generalizable and capable of exploring a broader design space, offering greater flexibility in generating innovative airfoil geometries that might not be achievable through latent space diffusion models like DiffAirfoil.

### 3 Method

This section outlines the method for developing the airfoil diffusion model. The first subsection details the airfoil training dataset, including data processing for model training. The second subsection explores the method for obtaining airfoil performance measurements. The third subsection presents the background theory of diffusion models and the formulation of the airfoil diffusion model.

**3.1 Dataset.** The UIUC Airfoil Database [16], hosted by the University of Illinois Urbana-Champaign, contains approximately 1600 airfoils, each represented by detailed coordinates.

Airfoil profiles in the UIUC database consist of varying numbers of  $(x, y)$  coordinate pairs. However, neural networks require uniform input dimensions, necessitating a standardized number of data points across all samples. To address this, we repanelized the airfoil profiles using Aerosandbox [17], interpolating each sample to a consistent set of 200 points via cubic splines. This approach preserves the airfoil's shape and characteristics while ensuring uniform data representation.

The airfoils are normalized such that  $x$ -coordinates range from 0 to 1 and  $y$ -coordinates from -1 to 1. After repanelization, all samples share identical  $x$ -coordinates, effectively reducing the problem dimensionality from two to one dimension, which simplifies both training and generation processes.

The  $y$ -coordinate values are structured as follows: The first 100 points, corresponding to  $x$ -values decreasing from 1 to 0, represent the upper surface of the airfoil, while the last 100 points, corresponding to  $x$ -values increasing from 0 to 1, represent the lower surface. During training, we organize these  $y$ -values into two channels to help the model differentiate between the upper and lower surfaces of the airfoils.

**3.2 Obtaining Aerodynamic Coefficients.** The performance of the airfoil is evaluated based on the lift and drag produced by the airfoil [18]. Lift is produced by the change in air velocity as it passes over the airfoil, while drag is created by skin friction and pressure changes due to flow separation and shocks [2].

**3.2.1 Airfoil Geometry.** The lift and drag produced by an airfoil are directly related to the shape of its profile [2]. The chord length is the straight line distance from the leading edge to the trailing edge of the airfoil. The camber represents the curvature of the profile and is defined as the line passing through the center of the airfoil, equidistant from the upper and lower surfaces. The airfoil thickness ratio is an additional feature of airfoils and is derived from the chord length  $c$  and maximum thickness  $t$  of the airfoil [2]:

$$\text{Airfoil Thickness Ratio} = \frac{t}{c}$$

The angle of attack  $\alpha$  is the angle between the chord line of the airfoil and the vector representing the relative motion of the airfoil through the air. This angle influences the lift and drag experienced by the airfoil by affecting the airflow over its surface [19].

To evaluate the aerodynamic performance of both the training and the synthesized airfoil profiles, we utilized NeuralFoil [20], a neural network-based tool designed to predict aerodynamic coefficients. NeuralFoil provides an efficient and accurate means of obtaining the coefficient of lift ( $C_l$ ) and the coefficient of drag ( $C_d$ ) for a given airfoil geometry.

**3.2.2 NeuralFoil Overview.** NeuralFoil leverages a deep learning model trained on a comprehensive dataset of airfoil shapes and their corresponding aerodynamic coefficients. This model is able to predict  $C_l$  and  $C_d$  based on the input airfoil coordinates. Using NeuralFoil, we can quickly assess the performance characteristics of a large number of airfoil profiles without the need for time-consuming computational fluid dynamics (CFD) simulations [20].

**3.2.3 Process for Obtaining Coefficients.** For each airfoil profile in our dataset, we followed these steps to obtain the aerodynamic coefficients.

- (1) **Preparation of Input Data:** Each airfoil profile, represented by 200 points along the  $x$  and  $y$  coordinates, was formatted as required by NeuralFoil.
- (2) **Prediction Using NeuralFoil:** The prepared airfoil data was fed into NeuralFoil, which predicted the corresponding  $C_l$  and  $C_d$  values.
- (3) **Post-Processing:** The predicted  $C_l$  and  $C_d$  values were recorded and used for further analysis. These coefficients were essential for filtering the synthesized airfoils and evaluating their performance characteristics.

**3.3 Denoising Diffusion Probabilistic Models (DDPMs).** DDPMs [7,21–25] are a class of probabilistic models inspired by nonequilibrium thermodynamics [26]. These models learn to reverse the iterative corruption process applied to the training data. The training procedure consists of two main phases:

- (1) The forward diffusion process.
- (2) The reverse diffusion process.

**3.3.1 Forward Process.** During the forward diffusion process, the training data are gradually corrupted until they approximate Gaussian noise. This corruption is achieved using a Markovian process [6,7,21–24], where the probability of each event depends only on the state of the previous event. In other words, the next future state depends only on the current state [23]. In our Airfoil diffusion model, the data distribution at step  $t$  is given by:

$$q(y_t|y_{t-1}) = \mathcal{N}\left(y_t; \sqrt{1 - \beta_t} \cdot y_{t-1}, \beta_t \cdot \mathbf{I}\right) \quad (1)$$

$$t \in (0, 1, \dots, T)$$

$$\beta_1, \beta_2, \dots, \beta_T \in [0, 1)$$

Here,  $q(y_0)$  represents the original data distribution. As  $t \rightarrow T$ ,  $q(y_t)$  approaches a Gaussian distribution. The variance schedule  $\beta_t$  is a hyperparameter.  $\mathcal{N}(y; \mu, \sigma)$  represents the normal distribution with mean  $\mu$  and covariance  $\sigma$  that produces  $y$  [21].

While the Markovian process is defined step-by-step, we improve computational efficiency by leveraging the following properties:

- (1) Each step in the process adds Gaussian noise.
- (2) The sum of Gaussian distributions is also Gaussian [27].

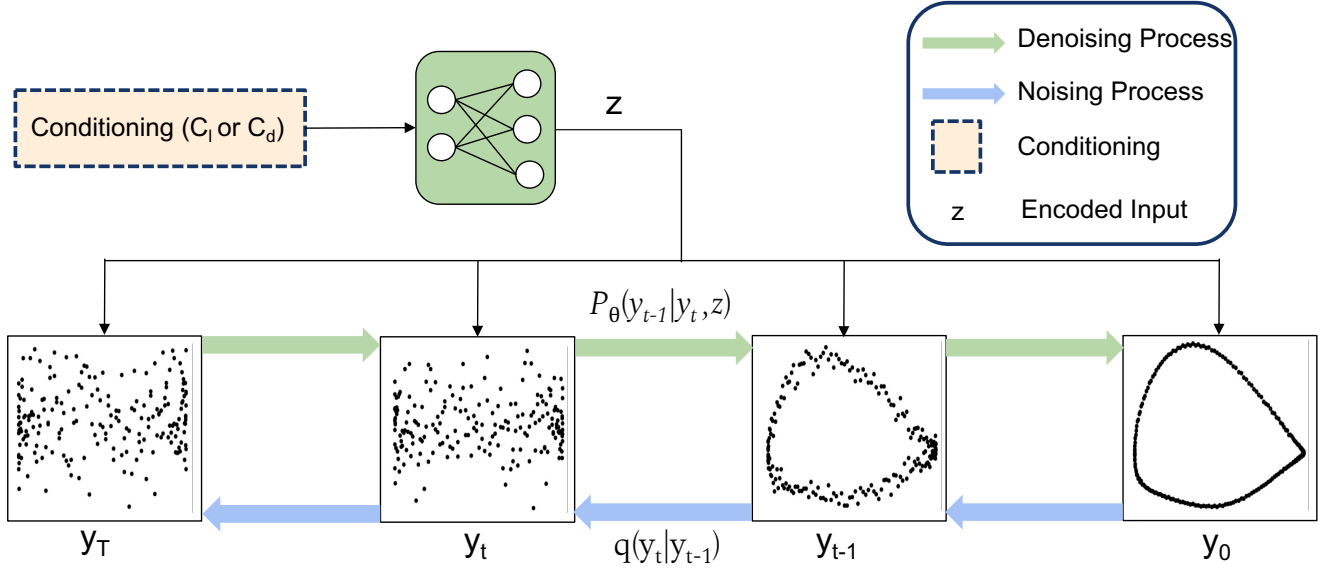


**Fig. 2** The conditioning input, such as  $C_d$  or  $C_l$  is fed through several multilayer perceptron layers to generate a context vector  $z$  for conditioning the diffusion model. In the forward process, the sample  $y$  coordinates are subjected to noise for  $T$  timesteps, gradually approaching gaussian noise. During the backward process, the model learns to estimate the added noise at each timestep  $t$  given conditioning  $z$  and  $y_t$ .

Substituting:

$$\alpha_t = 1 - \beta_t \quad (2)$$

$$\bar{\alpha}_t = \prod_{s=1}^t \alpha_s \quad (3)$$

$$\epsilon \sim \mathcal{N}(0, 1) \quad (4)$$

We define our sample and data distribution as follows:

$$y_t = \sqrt{\bar{\alpha}_t} y_0 + \sqrt{1 - \bar{\alpha}_t} \epsilon \quad (5)$$

$$q(y_t | y_0) = \mathcal{N}(y_t; \sqrt{\bar{\alpha}_t} y_0, (1 - \bar{\alpha}_t) \mathbf{I}) \quad (6)$$

**3.3.2 Reverse Process.** Starting from a random sample from the distribution defined in the forward process, we generate new airfoil samples within the original training data distribution [21–23]. This stepwise process is represented by the following distribution:

$$p_\theta(y_{t-1} | y_t) = \mathcal{N}(y_{t-1}; \mu_\theta(y_t, t), \Sigma_\theta(y_t, t)) \quad (7)$$

By substituting equations (2-4), we obtain our reconstructed data distribution and individual sample:

$$p_\theta(y_{t-1} | y_t) = \mathcal{N}\left(y_{t-1}; \frac{1}{\sqrt{\alpha_t}} \left(y_t - \frac{\beta_t}{\sqrt{1 - \bar{\alpha}_t}} \epsilon_\theta(y_t, t)\right), \beta_t \mathbf{I}\right) \quad (8)$$

$$y_{t-1} = \frac{1}{\sqrt{\alpha_t}} \left(y_t - \frac{\beta_t}{\sqrt{1 - \bar{\alpha}_t}} \epsilon_\theta(y_t, t)\right) + \sqrt{\beta_t} \epsilon \quad (9)$$

**3.3.3 Airfoil Diffusion.** The airfoil diffusion model generates novel airfoils by transforming random one-dimensional vectors through a trained neural network. This model allows for the generation of an arbitrary number of novel airfoils, limited only by the available computational power.

The forward diffusion process gradually adds Gaussian noise to an airfoil sample from the dataset, based on a predefined noise schedule  $q(y_t | y_{t-1})$ , until the sample approximates Gaussian noise. In contrast, the reverse process involves gradually removing the noise from a noised sample to reconstruct an approximation of the original airfoil.

This denoising process is performed by a neural network trained to predict the noise added at each time step. By learning to predict the added noise, the network effectively maps random vectors of length 200 to various airfoil geometries.

To predict the noise added to the samples, we used the U-net architecture [23,24,28]. The U-net functions similarly to an auto-encoder [29], where complex data is encoded into a latent representation and then decoded back. In our application, a noised sample is passed to the U-net along with timestep information. The U-net encodes the sample into a latent space and, using skip connections [28], retains information to aid in the decoding process. The output of the U-net is the predicted noise vector that was added to the input sample.

**3.4 Conditional Diffusion.** While standard diffusion models are effective at generating novel airfoil samples, they typically lack mechanisms to ensure that these generated samples adhere to specific geometric or performance-based criteria. To address this limitation, we incorporate a conditional diffusion model enhanced with classifier-free guidance, a technique that allows the generation process to be steered towards desired outcomes based on conditioning parameters, such as geometric features or aerodynamic performance metrics [6,7,30,31].

**3.4.1 Conditioning Mechanism.** The core idea behind the conditional diffusion model is to integrate additional information, such as specific geometric constraints or aerodynamic coefficients, directly into the generative process. This conditioning is achieved by processing the conditioning data (e.g., desired lift coefficient  $C_l$ , drag coefficient  $C_d$ , maximum thickness, etc.) through a set of linear transformations, which map the conditioning information into a high-dimensional embedding space. Specifically, the conditioning information is passed through two fully connected (linear) layers followed by a ReLU activation function to produce a conditioning embedding.

This embedding is then fused with the timestep information (representing the current state of the diffusion process) using a bilinear layer. The bilinear layer combines the time and conditioning embeddings into a single representation that captures both the progression of the diffusion process and the target constraints.

**3.4.2 Integration into the U-Net Architecture.** To effectively leverage the conditioning information during the generation process, we employ a Conditional U-Net architecture. The U-Net is a well-suited architecture for this task due to its ability to capture and retain spatial information at various scales through its encoder-decoder structure, enhanced with skip connections that prevent the loss of fine-grained details.

In our Conditional U-Net, the fused embedding (containing both the conditioning and timestep information) is injected into each block of the U-Net, ensuring that the model consistently takes the conditioning criteria into account throughout the diffusion process. This design enables the model to learn the relationship between the airfoil’s geometry and the specified conditioning parameters, allowing for the generation of airfoils that meet specific aerodynamic or geometric requirements.

As the diffusion model iteratively refines the airfoil from a noisy sample, the conditioning information guides the model to prioritize designs that align with the target specifications. This method not only improves the relevance of the generated airfoils but also enhances the model’s ability to explore feasible designs within the conditioned space.

**3.4.3 Application of Classifier-Free Guidance.** Classifier-free guidance is a critical component of our conditional diffusion model. Traditional approaches to conditional generation often rely on an external classifier to steer the generative process towards desired outcomes. However, this approach can be cumbersome and may introduce additional complexity and training requirements. Instead, we use classifier-free guidance, which allows the model to simultaneously learn the diffusion process with and without conditioning inputs, effectively bypassing the need for a separate classifier.

During training, the model occasionally drops the conditioning inputs and learns to generate airfoils unconditionally. By doing so, the model develops an internal understanding of the target distribution both with and without conditioning, enabling it to use this knowledge to adjust the strength of conditioning during generation. This approach provides a more flexible and efficient means of controlling the generation process, allowing us to fine-tune the balance between adhering to the conditioning criteria and exploring novel airfoil designs.

**3.4.4 Conditioning on Aerodynamic Coefficients.** To further enhance the control over the generated airfoil profiles, we condition the model on aerodynamic coefficients such as  $C_l$  and  $C_d$ , which are predicted using the NeuralFoil tool [20]. By incorporating these performance metrics directly into the conditioning mechanism, our model can generate airfoils tailored to specific aerodynamic requirements, such as maximizing lift or minimizing drag under certain operating conditions.

The inclusion of these aerodynamic coefficients as conditioning parameters adds another layer of flexibility to our diffusion model, enabling the generation of airfoils that not only adhere to geometric constraints but also meet specific performance targets. This capability is particularly valuable in practical design applications where achieving optimal aerodynamic performance is paramount.

**3.4.5 Summary.** The conditional diffusion model developed in this work provides a powerful and flexible framework for generating airfoil profiles that meet specific geometric and aerodynamic criteria. By integrating classifier-free guidance and conditioning on performance metrics, our approach addresses the limitations of traditional diffusion models, offering a robust solution for aerodynamic shape optimization.

**3.5 Shape Similarity Measurement.** To evaluate the similarity between the generated airfoils and the training dataset, we utilized the Chamfer distance [32,33], a metric commonly used in shape analysis to quantify the dissimilarity between two sets of points. The Chamfer distance is calculated by summing the average of the minimum Euclidean distances from each point in the first set to the nearest point in the second set, and vice versa. Mathematically, the Chamfer distance between two point sets  $A$  and  $B$  is defined as:

$$d_{\text{Chamfer}}(A, B) = \frac{1}{|A|} \sum_{a \in A} \min_{b \in B} \|a - b\|_2 + \frac{1}{|B|} \sum_{b \in B} \min_{a \in A} \|b - a\|_2 \quad (10)$$

A lower Chamfer distance indicates a higher similarity between the airfoils, while a higher distance suggests greater diversity. The distances were calculated using PyTorch on a GPU to efficiently handle the large datasets involved.

## 4 Results and Discussion

In this section, we explore the performance and capabilities of the Airfoil Diffusion model, trained on the UIUC airfoil database, through both unconditional and conditional generation. The results are analyzed based on geometric properties, aerodynamic performance, and the novelty of the generated airfoil profiles.

**4.1 Unconditional Generation.** To assess the capabilities of the unconditional Airfoil Diffusion model, 2000 random samples were generated by feeding random vectors into the model. The output airfoil profiles were evaluated based on their geometric and aerodynamic properties, and the resulting distributions of lift coefficient ( $C_l$ ), drag coefficient ( $C_d$ ), maximum camber, and maximum thickness were compared with those from the UIUC dataset. Figure 3 presents histograms of these distributions.

The generated airfoils exhibit a narrower range of  $C_l$  values, ranging from -0.1 to 0.5, compared to the broader range of -0.2 to 1.25 observed in the UIUC dataset. Similarly, the  $C_d$  values for the generated airfoils span from 0.001 to 0.009, whereas the UIUC dataset shows a range from 0.001 to 0.015. In terms of geometric properties, the generated airfoils have maximum camber values between 0 and 0.05 and maximum thickness between 0.01 and 0.13, which are more constrained compared to the UIUC dataset (0 to 0.1 for camber and 0.01 to 0.35 for thickness).

The narrower distributions and the leftward shift in means for all properties suggest that the model tends to generate airfoils that are more conservative and less extreme than those in the UIUC dataset. Specifically, the underrepresentation of high  $C_l$  and  $C_d$  values, as well as extreme thickness and camber, indicates that the model may favor the generation of more typical airfoil shapes rather than exploring the full range of geometries present in the training set. This behavior could be attributed to the inherent biases in the training data distribution or the diffusion process, which might favor the generation of profiles closer to the dataset’s mean.

**4.2 Conditional Generation.** The conditional diffusion model was evaluated by generating 1000 samples conditioned on specific values of  $C_l$  and  $C_d$ . Two separate models were trained: one conditioned on  $C_d$  and the other on  $C_l$ . The input conditioning values were linearly spaced between the minimum and maximum values of  $C_d$  and the minimum and twice the maximum of  $C_l$  in the UIUC dataset (Table 1) to test the model’s potential to generate samples with greater  $C_l$  values.

The accuracy of the generated profiles was assessed by comparing the percent difference between the input conditioning values and the corresponding evaluated values using NeuralFoil. Figure 4 a) shows boxplots of the percent differences, highlighting the model’s performance in adhering to the conditioning parameters.

The  $C_l$ -conditioned model exhibits a wider range of percent differences with a standard deviation of 13.15, indicating a greater

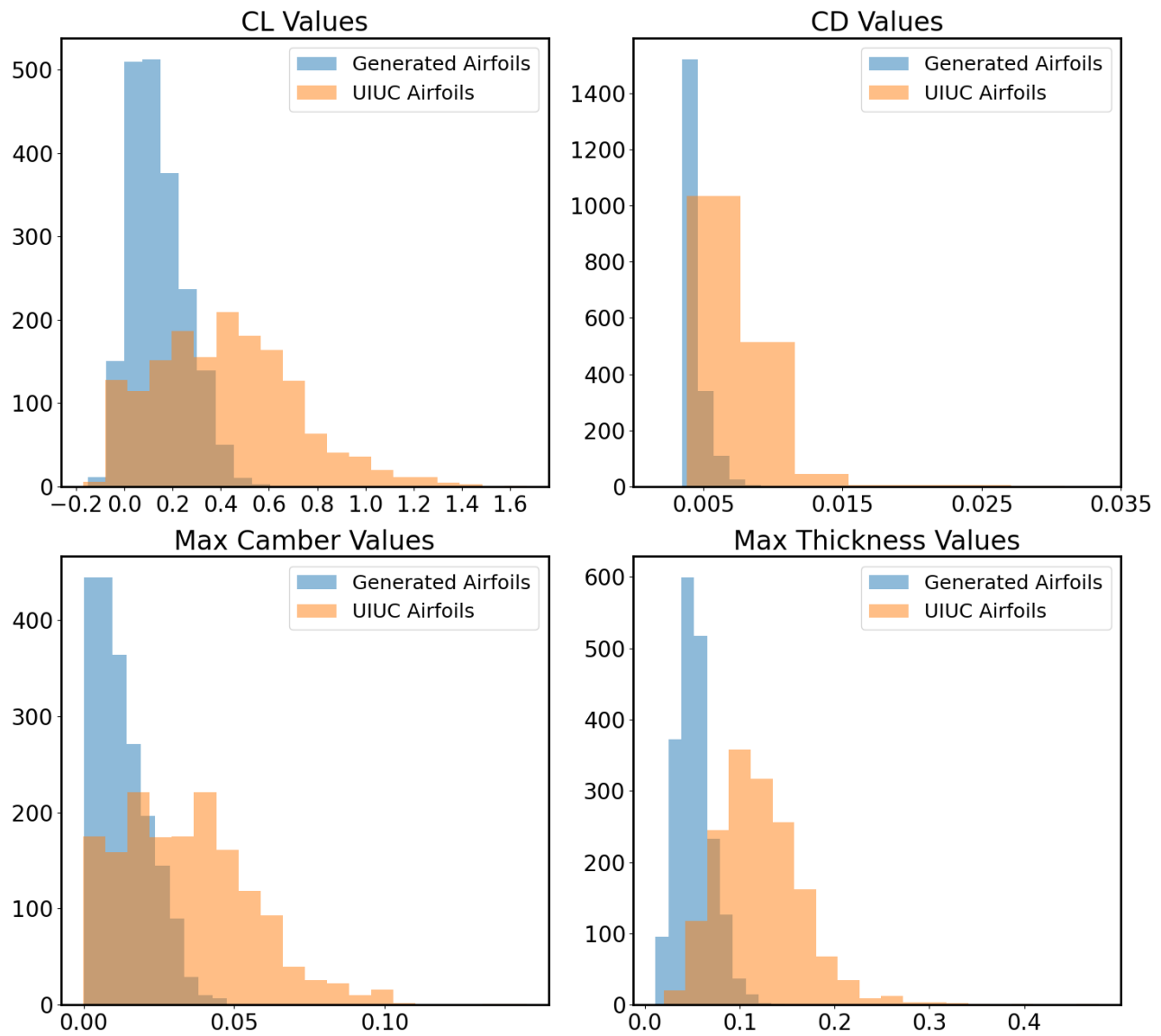


**Fig. 3** Histograms of  $C_l$ ,  $C_d$ , maximum camber, and maximum thickness for the UIUC and generated samples. The generated samples exhibit narrower distributions compared to the UIUC data, with their means slightly shifted to the left of the UIUC distributions.

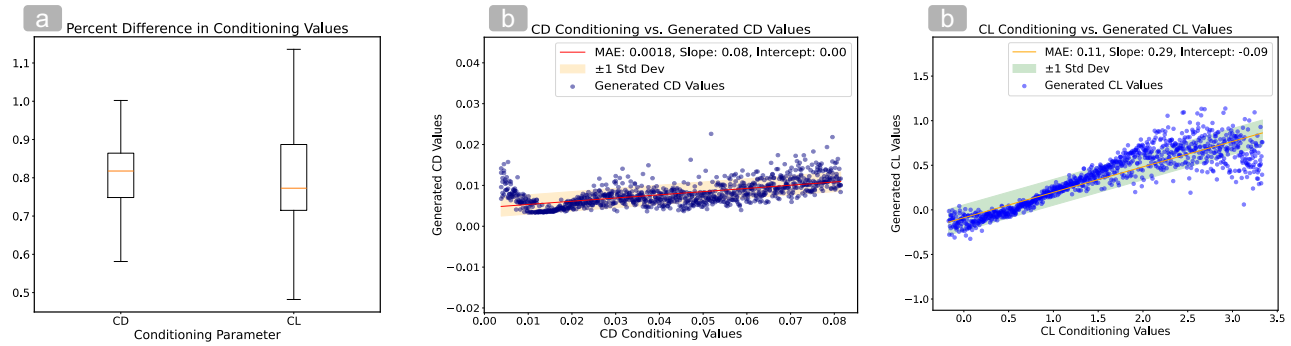


**Fig. 4** a) Box plots of the percent difference between the input conditioning values for  $C_l$  and  $C_d$  and the corresponding evaluated values of generated profiles. Scatter plots of the relationship between input conditioning values for  $C_d$  and  $C_l$  in (b) and (c), respectively. Also shown are the lines of best fit, along with the visual representation of the standard deviation from the line of best fit.

Property	Maximum	Minimum
$C_d$	0.0814	0.0038
$C_l$	1.6670	-0.1701

**Table 1** Min and max values of  $C_l$  and  $C_d$  in the UIUC dataset.

variability in the accuracy of the generated profiles. In contrast, the  $C_d$ -conditioned model demonstrates more consistent performance, with a lower standard deviation of 0.19. This suggests that while the  $C_l$ -conditioned model is more flexible in generating a diverse set of airfoils, it may struggle to precisely match the desired  $C_l$  values, potentially due to the higher complexity of the lift coefficient's dependence on airfoil geometry.

Conditioning Parameter	Median	Standard Deviation
$C_d$	0.8176	0.1960
$C_l$	0.8578	13.15

**Table 2** Median and standard deviation values for the box plots in Fig. 4 a). The  $C_l$ -conditioned model exhibits a broader distribution, as indicated by its greater standard deviation.

Further analysis of the relationship between the conditioned and generated values was conducted by plotting scatter plots of the input conditioning values against the NeuralFoil-evaluated results (Fig. 4 b), a)). The mean absolute error (MAE) was calculated to quantify the accuracy of the conditioning. The  $C_d$ -conditioned model achieved an MAE of 0.0018, whereas the  $C_l$ -conditioned model had a higher MAE of 0.04. The slope of the best-fit line for the  $C_d$ -conditioned model was 0.08, compared to 0.29 for the  $C_l$ -conditioned model, indicating that the  $C_d$ -conditioned model's outputs were less sensitive to the input conditioning values. As the  $C_l$  conditioning values exceeded the values seen in the UIUC samples, the  $C_l$  conditioned model generations produced a greater range of  $C_l$  evaluation values from generations, however the model still tended to produce airfoils with greater  $C_l$  values corresponding to increasing conditioning values. This effect is likely due to passing conditioning values to the model that were not seen in training samples.

The range of output  $C_d$  values was 0.0033 to 0.0226, and the range of output  $C_l$  values was -0.3319 to 0.6068, compared to the input conditioning ranges of 0.038 to 0.0814 and -0.1701 to 3.21, respectively. The bias observed in the conditional diffusion model, particularly the narrower output range for  $C_l$  values, may be attributed to the distribution of samples in the UIUC dataset, where most airfoils have  $C_l$  values between -0.1 and 0.6, and  $C_d$  values between 0.002 and 0.015. The model's tendency to generate air-

foils with more typical characteristics rather than extreme outliers suggests a limitation in exploring the full range of possible airfoil geometries.

**4.2.1 Aerodynamic Performance.** Evaluating the aerodynamic performance of the generated airfoils is crucial, extending beyond merely targeting specific  $C_d$  and  $C_l$  values. The lift-to-drag ratio ( $C_l/C_d$ ) is a key metric that provides a comprehensive assessment of an airfoil's efficiency [3,34].

Figure 5(a) presents a scatter plot of the evaluated  $C_d$  and  $C_l$  values for both the  $C_d$ -conditioned and  $C_l$ -conditioned models. The  $C_d$ -conditioned model exhibits a broader range of  $C_d$  values, demonstrating its ability to generate airfoils with diverse drag characteristics. However, it produces a narrower range of  $C_l$  values, indicating more constrained lift performance. Conversely, the  $C_l$ -conditioned model generates a broader spectrum of  $C_l$  values, showcasing its capacity to explore varied lift characteristics, while producing airfoils with a narrower range of  $C_d$  values, favoring lower drag. This bias towards lower drag in the  $C_l$ -conditioned model is advantageous for maximizing the lift-to-drag ratio, making it particularly effective in producing efficient airfoil designs.

Figure 5(c) compares the lift-to-drag ratios for the  $C_d$ - and  $C_l$ -conditioned models against the UIUC dataset through box plots. The  $C_d$ -conditioned model demonstrates the narrowest range of lift-to-drag ratios, indicating a more consistent yet potentially less exploratory design space. In contrast, the  $C_l$ -conditioned model shows a wider range of lift-to-drag ratios, with some generated airfoils exceeding the maximum ratios observed in the UIUC dataset. This result highlights the  $C_l$ -conditioned model's ability to generate airfoils with superior aerodynamic performance, surpassing the capabilities of existing designs within the training data. These outcomes underscore the model's potential in advancing airfoil design by pushing aerodynamic efficiency beyond conventional limits.

Figure 5(b) presents the airfoils with the greatest lift-to-drag ratios from the  $C_l$ -conditioned model (green) and UIUC dataset (red). The top two UIUC airfoils have lift-to-drag ratios of 175.28 and 166.12. Both profiles are characterized by elongated shapes with minimal thickness. The profile with a lift-to-drag ratio of 166.12 exhibits significant camber and an extremely thin profile starting from approximately one-third of the chord length to the trailing edge. The profile with a lift-to-drag ratio of 175.28 is slightly thicker, with less camber, tapering sharply in thickness towards the trailing edge. Similarly, the top two airfoils from the  $C_l$ -conditioned model exhibit relatively little thickness. The profile with a lift-to-drag ratio of 183.76 is slightly thicker than the UIUC sample with a ratio of 166.12, with extremely thin thickness starting at approximately the last third of the chord length, and slightly less camber. The profile with a lift-to-drag ratio of 189.39 is distinct, with the greatest thickness among the samples and less overall

camber. The lower half of this profile has a relatively straight section for the middle two-thirds of the chord, with slight camber at the leading and trailing edges. The upper half has moderate camber with a slight increase at the leading and trailing edges.

From the lift-to-drag ratio comparison between the conditioned models and the UIUC dataset, it is evident that the  $C_l$ -conditioned model is capable of generating airfoils with performance characteristics that surpass those found in the training samples. This finding highlights the applicability of conditional airfoil diffusion models in real-world aerodynamic design, offering the potential to enhance the efficiency of future airfoil designs.

**4.2.2 Novelty of Generation.** To quantify the novelty of the generated airfoils, we calculated the Chamfer Distance between the profiles generated by the  $C_l$  and  $C_d$ -conditioned models and the closest matching profiles from the UIUC dataset. The boxplots in Figure 6 illustrate the distribution of Chamfer Distances for both models, indicating that the generated airfoils have a significant degree of novelty, as they differ considerably from the existing profiles in the UIUC dataset.

The Chamfer Distance values for both models are generally clustered between 0.7 and 0.95, which indicates that the generated airfoils maintain a reasonable level of similarity to the training set while still exhibiting notable differences. This range also suggests that while the model is capable of generating novel airfoils, it remains somewhat anchored to the existing design space defined by the UIUC dataset.

Notably, the Chamfer Distance distributions for both models do not extend below 0.6, nor do they exceed 1.0, aligning well with the range of  $y$ -values in the training dataset, which spans from -0.21 to 0.27. This constraint likely reflects the influence of the diffusion process and conditioning, which help the model generate realistic airfoils that avoid extreme deviations from the known design space. However, the upper end of the Chamfer Distance distribution approaching 1.0 indicates that some generated airfoils are indeed pushing the boundaries of the existing dataset, suggesting the model's potential for creating innovative designs.

The slightly higher Chamfer Distances observed in the  $C_d$ -conditioned model, compared to the  $C_l$ -conditioned model, suggest that the  $C_d$  model may be more effective in exploring the geometric space beyond what is represented in the training dataset. This could be due to the broader range of drag characteristics that the model is conditioned on, which might encourage more variation in the resulting airfoil shapes. In contrast, the  $C_l$ -conditioned model, while still generating novel airfoils, appears to be more conservative in its exploration of new geometries, likely due to the more constrained range of lift values it is conditioned on.

Overall, these results indicate that the conditional diffusion model is capable of generating airfoils that are distinct from those in the training dataset, with the potential to introduce novel and potentially more efficient aerodynamic shapes. However, the model's novelty is tempered by its tendency to produce airfoils that remain within a realistic and aerodynamically viable design space.

## 5 Conclusion

In this paper, we presented a novel diffusion-based framework for airfoil design, leveraging the UIUC airfoil database to train a model capable of generating a wide variety of airfoil profiles. By conditioning the generation process on specific aerodynamic coefficients such as lift ( $C_l$ ) and drag ( $C_d$ ), our model demonstrated the ability to produce airfoils that meet desired aerodynamic and geometric criteria with high fidelity.

Our experiments revealed that the diffusion model is effective not only in generating airfoils that align well with the overall distribution of the training dataset but also in producing designs that push the boundaries of conventional airfoil geometries. The unconditional generation results showed a tendency towards conservative designs, while the conditional generation results highlighted the model's flexibility in achieving specific performance targets, with the  $C_l$ -conditioned model excelling in generating airfoils with superior lift-to-drag ratios.

One of the key strengths of our approach lies in its capacity to produce novel airfoil geometries, as evidenced by the Chamfer Distance analysis. The generated airfoils, while grounded in the characteristics of the training data, exhibit significant novelty, indicating the model's potential for discovering innovative aerodynamic shapes. Importantly, the generated designs remain within a realistic and aerodynamically viable space, ensuring their practical applicability.

In summary, the diffusion model-based framework we introduced represents a powerful tool for expanding the design space and discovering new, high-performance airfoil shapes. Future work could explore extending this methodology to three-dimensional aerodynamic shapes, integrating multiple conditioning parameters within a single model, and applying this generative approach to other domains where innovative design solutions are critical.



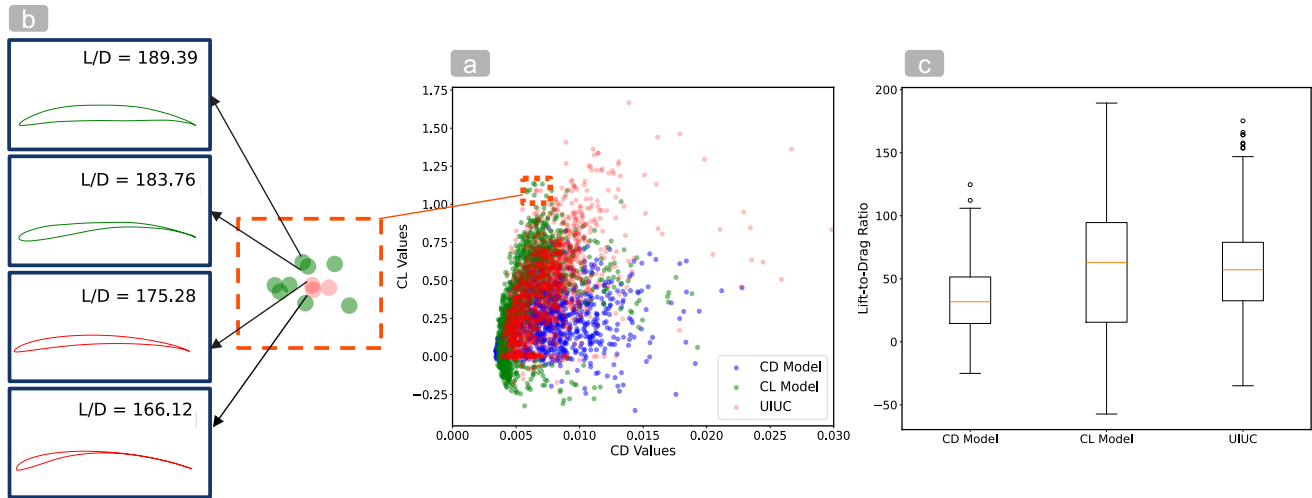


**Fig. 5** a) Scatter plot of the  $C_d$  (x-axis) and  $C_l$  (y-axis) values from NeuralFoil evaluations for both the  $C_d$ -conditioned (blue points) and  $C_l$ -conditioned (green points) models. The  $C_d$ -conditioned model spans a broader range of  $C_d$  values, while the  $C_l$ -conditioned model spans a broader range of  $C_l$  values, with a bias towards lower  $C_d$  values. b) Airfoils with the greatest lift-to-drag ratios from the  $C_l$ -conditioned model (green) and UIUC dataset (red). The top UIUC airfoils have elongated shapes with minimal thickness and varying degrees of camber, while the  $C_l$ -conditioned model generates airfoils that similarly exhibit reduced thickness and differing camber profiles. The  $C_l$ -conditioned airfoils generally achieve higher lift-to-drag ratios with slightly more thickness and less camber compared to the UIUC samples. c) Box plots of the lift-to-drag ratio for the  $C_d$ - and  $C_l$ -conditioned models and the UIUC dataset. The  $C_l$ -conditioned model exhibits a wider range of lift-to-drag ratios and produces samples with greater lift-to-drag ratios than those seen in the UIUC dataset.

## Acknowledgment

### Nomenclature

- $x$  = Horizontal coordinate of airfoil profile
- $y$  = Vertical coordinate of airfoil profile
- $c$  = Chord length
- $t$  = Maximum thickness of the airfoil
- $t/c$  = Airfoil thickness ratio
- $\alpha$  = Angle of attack
- $C_l$  = Coefficient of lift
- $C_d$  = Coefficient of drag
- $\mathcal{N}(\mu, \sigma)$  = Normal distribution with mean  $\mu$  and covariance  $\sigma$
- $q(y_t|y_{t-1})$  = Probability of  $y_t$  given  $y_{t-1}$  in the forward diffusion process
- $\beta_t$  = Variance schedule at step  $t$
- $\alpha_t$  = 1 minus  $\beta_t$
- $\tilde{\alpha}_t$  = Product of  $\alpha_s$  from 1 to  $t$
- $\epsilon$  = Gaussian noise
- $p_\theta(y_{t-1}|y_t)$  = Probability of  $y_{t-1}$  given  $y_t$  in the reverse process
- $\mu_\theta(y_t, t)$  = Mean of the predicted distribution in the reverse process
- $\Sigma_\theta(y_t, t)$  = Covariance of the predicted distribution in the reverse process
- $y_0$  = Original data distribution
- $y_t$  = Data distribution at step  $t$

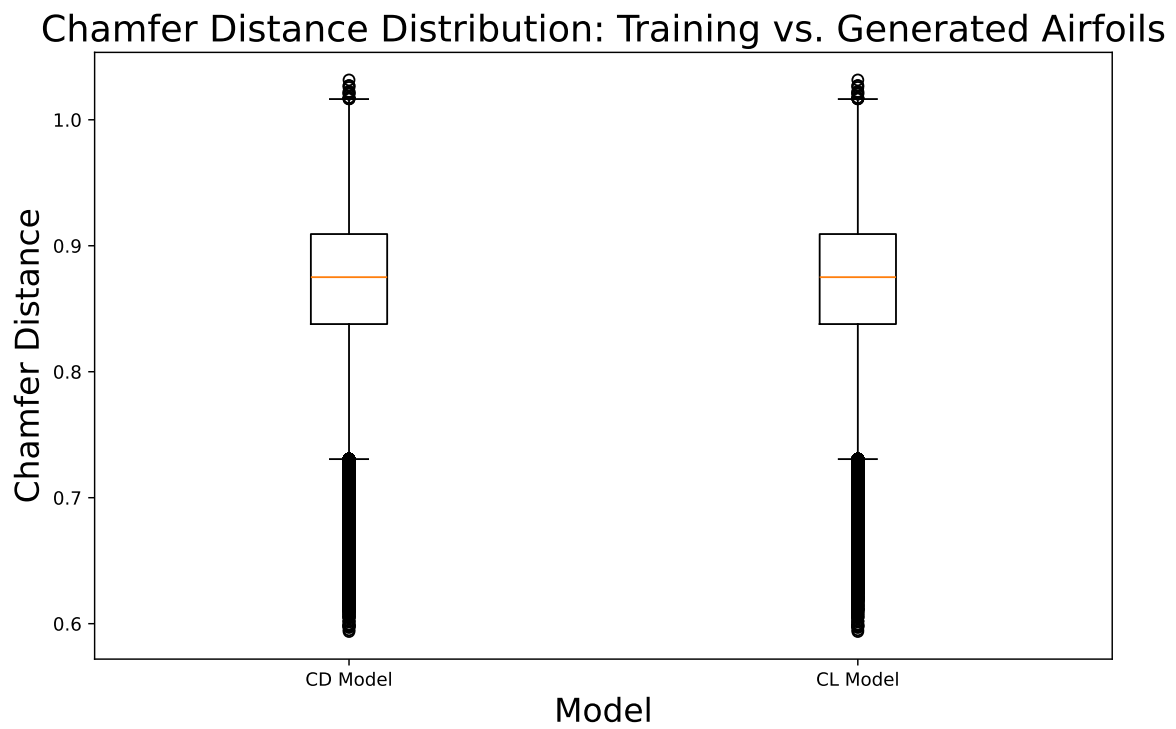


**Fig. 6** Boxplots of the Chamfer Distance between the UIUC dataset samples and the  $C_d$  and  $C_l$  conditioned models.

## References

- [1] Wang, L., Zhang, H., Wang, C., Tao, J., Lan, X., Sun, G., and Feng, J., 2024, "A Review of Intelligent Airfoil Aerodynamic Optimization Methods Based on Data-Driven Advanced Models," *Mathematics*, **12**(10).
- [2] Raymer, D. P., 2006, *Aircraft Design: A Conceptual Approach*, 4th ed., AIAA Education Series, American Institute of Aeronautics and Astronautics.
- [3] Wang, Y., Shimada, K., and Farimani, A., 2021, "Airfoil GAN: Encoding and Synthesizing Airfoils for Aerodynamic-aware Shape Optimization," *ArXiv*, **abs/2101.04757**.
- [4] Morris, A., Allen, C., and Rendall, T., 2008, "Wing Design by Aerodynamic and Aeroelastic Shape Optimisation," .
- [5] Hermans, M., Schrauwen, B., Bienstman, P., and Dambre, J., 2014, "Automated Design of Complex Dynamic Systems," *PLoS ONE*, **9**.
- [6] Jadhav, Y., Berthel, J., Hu, C., Panat, R., Beuth, J., and Farimani, A. B., 2023, "StressD: 2D Stress estimation using denoising diffusion model," *Computer Methods in Applied Mechanics and Engineering*, **416**, p. 116343.
- [7] Jadhav, Y., Berthel, J., Hu, C., Panat, R., Beuth, J., and Barati Farimani, A., 2024, "Generative Lattice Units with 3D Diffusion for Inverse Design: GLU3D," *Advanced Functional Materials*, p. 2404165.
- [8] Chen, W. and Ramamurthy, A., 2021, "Deep Generative Model for Efficient 3D Airfoil Parameterization and Generation," *ArXiv*, **abs/2101.02744**.
- [9] Xie, H., Wang, J., and Zhang, M., 2022, "Soft and Hard Constrained Parametric Generative Schemes for Encoding and Synthesizing Airfoils," *ArXiv*, **abs/2205.02458**.
- [10] Barrett, T. R., Bressloff, N., and Keane, A., 2006, "Airfoil shape design and optimization using multifidelity analysis and embedded inverse design," *AIAA Journal*, **44**, pp. 2051–2060.
- [11] Zhang, Y. and Joo, S., 2020, "Optimizing Airfoil Shape Using B-Spline Curves," *Computers & Fluids*, **201**, p. 104468.
- [12] Mukesh, A. and Rathakrishnan, E., 2021, "Optimization of Airfoil Shapes Using B-Spline Curves and Genetic Algorithms," *Aerospace Science and Technology*, **110**, p. 106501.
- [13] Li, J., Zhang, M., and Martins, J. R. R. A., 2020, "Efficient Aerodynamic Shape Optimization with Deep-Learning-Based Geometric Filtering," *AIAA Journal*, **58**(10), pp. 4243–4259.
- [14] Wei, Z., Guillard, B., Bauerheim, M., Chapin, V., and Fua, P., 2023, "Latent Representation of CFD Meshes and Application to 2D Airfoil Aerodynamics," *AIAA Journal*.
- [15] Wei, Z., Dufour, E., Pelletier, C., Fua, P., and Bauerheim, M., 2024, "DiffAirfoil: An Efficient Novel Airfoil Sampler Based on Latent Space Diffusion Model for Aerodynamic Shape Optimization," *AIAA AVIATION Forum*.
- [16] Selig, M., 1996, "UIUC airfoil data site," Department of Aeronautical and Astronautical Engineering University of Illinois at Urbana-Champaign, [http://m-selig.ae.illinois.edu/ads/coord\\_database.html](http://m-selig.ae.illinois.edu/ads/coord_database.html)
- [17] Sharpe, P. D., 2021, "AeroSandbox: A Differentiable Framework for Aircraft Design Optimization," Master's thesis, Massachusetts Institute of Technology.
- [18] Koning, W. J. F., Romander, E. A., Cummings, H. V., Perez Perez, B. N., and Buning, P. G., 2023, "On Improved Understanding of Airfoil Performance Evaluation Methods at Low Reynolds Numbers," *Journal of Aircraft*.
- [19] Gracey, W., 1958, "Summary of methods of measuring angle of attack on aircraft," National Advisory Committee for Aeronautics, *Technical Note 4351*.
- [20] Sharpe, P., 2023, "NeuralFoil: An airfoil aerodynamics analysis tool using physics-informed machine learning," <https://github.com/peterdsharpe/NeuralFoil>.
- [21] Croitoru, F.-A., Hondru, V., Ionescu, R. T., and Shah, M., 2022, "Diffusion Models in Vision: A Survey," *IEEE Transactions on Pattern Analysis and Machine Intelligence*, **45**, pp. 10850–10869.
- [22] Ho, J., Saharia, C., Chan, W., Fleet, D. J., Norouzi, M., and Salimans, T., 2021, "Cascaded Diffusion Models for High Fidelity Image Generation," *J. Mach. Learn. Res.*, **23**, pp. 47:1–47:33.
- [23] Ho, J., Jain, A., and Abbeel, P., 2020, "Denoising Diffusion Probabilistic Models," *arXiv preprint arxiv:2006.11239*.
- [24] Ogoke, F., Liu, Q., Ajenifujah, O., Myers, A., Quirarte, G., Beuth, J., Malen, J., and Farimani, A. B., 2023, "Inexpensive High Fidelity Melt Pool Models in Additive Manufacturing Using Generative Deep Diffusion," **2311.16168**
- [25] Yang, L., Zhang, Z., Hong, S., Xu, R., Zhao, Y., Shao, Y., Zhang, W., Yang, M.-H., and Cui, B., 2022, "Diffusion Models: A Comprehensive Survey of Methods and Applications," *ACM Computing Surveys*, **56**, pp. 1 – 39.
- [26] Sohl-Dickstein, J., Weiss, E. A., Maheswaranathan, N., and Ganguli, S., 2015, "Deep Unsupervised Learning using Nonequilibrium Thermodynamics," **1503.03585**
- [27] DeGroot, M. H. and Schervish, M. J., 2014, *Probability and Statistics*, 4th ed., Pearson, Boston.
- [28] Ronneberger, O., Fischer, P., and Brox, T., 2015, "U-Net: Convolutional Networks for Biomedical Image Segmentation," **1505.04597**, <https://arxiv.org/abs/1505.04597>
- [29] Bank, D., Koenigstein, N., and Giryes, R., 2020, "Autoencoders," *ArXiv*, **abs/2003.05991**.
- [30] Ho, J. and Salimans, T., 2022, "Classifier-Free Diffusion Guidance," **2207.12598**, <https://arxiv.org/abs/2207.12598>
- [31] Hu, B., Layton, A., and Chen, H., 2024, "Drug Discovery SMILES-to-Pharmacokinetics Diffusion Models with Deep Molecular Understanding," **2408.07636**, <https://arxiv.org/abs/2408.07636>
- [32] Barrow, H., Tenenbaum, J., Bolles, R., and Wolf, H., 1977, "Parametric correspondence and chamfer matching: Two new techniques for image matching," *Proceedings of the International Joint Conference on Artificial Intelligence*, pp. 659–663.
- [33] Lin, C. and Zhang, H., 2023, "Hyperbolic Chamfer Distance for Point Cloud Completion," *Proceedings of the IEEE/CVF International Conference on Computer Vision (ICCV)*, pp. 2292–2300, [https://openaccess.thecvf.com/content/ICCV2023/papers/Lin\\_Hyperbolic\\_Chamfer\\_Distance\\_for\\_Point\\_Cloud\\_Completion\\_ICCV\\_2023\\_paper.pdf](https://openaccess.thecvf.com/content/ICCV2023/papers/Lin_Hyperbolic_Chamfer_Distance_for_Point_Cloud_Completion_ICCV_2023_paper.pdf)
- [34] Akram, M. T. and Kim, M.-H., 2021, "Aerodynamic Shape Optimization of NREL S809 Airfoil for Wind Turbine Blades Using Reynolds-Averaged Navier Stokes Model—Part II," *Applied Sciences*, **11**(5), p. 2211.

**List of Figures**

1 Overview of the Airfoil Diffusion Model:  
a) Airfoil conditioning information such as the coefficient of lift ( $C_l$ ), coefficient of drag ( $C_d$ ), maximum thickness, and maximum camber is passed through b) conditional embedding multi-layer perceptron (MLP) layers. The embedded conditioning information is passed to e) the denoising U-Net. During training, samples are progressively distorted to approximate Gaussian noise, as shown in c). In the inference phase, a noise vector d) along conditioning value embedding are input to the U-Net e), which outputs the conditionally generated airfoil profile in d). . . . . 2

2 The conditioning input, such as  $C_d$  or  $C_l$  is fed through several multilayer perceptron layers to generate a context vector  $z$  for conditioning the diffusion model. In the forward process, the sample  $y$  coordinates are subjected to noise for  $T$  timesteps, gradually approaching gaussian noise. During the backward process, the model learns to estimate the added noise at each timestep  $t$  given conditioning  $z$  and  $y_t$ . . . . . 4

3 Histograms of  $C_l$ ,  $C_d$ , maximum camber, and maximum thickness for the UIUC and generated samples. The generated samples exhibit narrower distributions compared to the UIUC data, with their means slightly shifted to the left of the UIUC distributions. . . . . 6

4 a) Box plots of the percent difference between the input conditioning values for  $C_l$  and  $C_d$  and the corresponding evaluated values of generated profiles. Scatter plots of the relationship between input conditioning values for  $C_d$  and  $C_l$  in (b) and (c), respectively. Also shown are the lines of best fit, along with the visual representation of the standard deviation from the line of best fit. . . . . 7

5 a) Scatter plot of the  $C_d$  (x-axis) and  $C_l$  (y-axis) values from NeuralFoil evaluations for both the  $C_d$ -conditioned (blue points) and  $C_l$ -conditioned (green points) models. The  $C_d$ -conditioned model spans a broader range of  $C_d$  values, while the  $C_l$ -conditioned model spans a broader range of  $C_l$  values, with a bias towards lower  $C_d$  values. b) Airfoils with the greatest lift-to-drag ratios from the  $C_l$ -conditioned model (green) and UIUC dataset (red). The top UIUC airfoils have elongated shapes with minimal thickness and varying degrees of camber, while the  $C_l$ -conditioned model generates airfoils that similarly exhibit reduced thickness and differing camber profiles. The  $C_l$ -conditioned airfoils generally achieve higher lift-to-drag ratios with slightly more thickness and less camber compared to the UIUC samples. c) Box plots of the lift-to-drag ratio for the  $C_d$ - and  $C_l$ -conditioned models and the UIUC dataset. The  $C_l$ -conditioned model exhibits a wider range of lift-to-drag ratios and produces samples with greater lift-to-drag ratios than those seen in the UIUC dataset. . . . . 9

6 Boxplots of the Chamfer Distance between the UIUC dataset samples and the  $C_d$  and  $C_l$  conditioned models. . . . . 10

**List of Tables**

1 Min and max values of  $C_l$  and  $C_d$  in the UIUC dataset. . . . . 7

2 Median and standard deviation values for the box plots in Fig. 4 a). The  $C_l$ -conditioned model exhibits a broader distribution, as indicated by its greater standard deviation. . . . . 7